
TELECONNECTION PATTERNS OF DIFFERENT EL NIÑO TYPES REVEALED BY CLIMATE NETWORK CURVATURE

A PREPRINT

Felix M. Strnad *

Cluster of Excellence Machine Learning: New Perspectives for Science
Universität Tübingen
72072 Tübingen, Germany

Jakob Schlör *

Cluster of Excellence Machine Learning: New Perspectives for Science
Universität Tübingen
72072 Tübingen, Germany

Christian Fröhlich

Cluster of Excellence Machine Learning: New Perspectives for Science
Universität Tübingen
72072 Tübingen, Germany

Bedartha Goswami

Cluster of Excellence Machine Learning: New Perspectives for Science
Universität Tübingen
72072 Tübingen, Germany

March 15, 2022

ABSTRACT

The diversity of El Niño events is commonly described by two distinct flavors, the Eastern Pacific (EP) and Central Pacific (CP) types. While the remote impacts, i.e. teleconnections, of EP and CP events have been studied for different regions individually, a global picture of their teleconnection patterns is still lacking. Here, we use Forman-Ricci curvature applied on climate networks constructed from 2-meter air temperature data to distinguish regional links from teleconnections. Our results confirm that teleconnection patterns are strongly influenced by the El Niño type. EP events have primarily tropical teleconnections whereas CP events involve tropical-extratropical connections, particularly in the Pacific. Moreover, the central Pacific region does not have many teleconnections, even during CP events. It is mainly the eastern Pacific that mediates the remote influences for both El Niño types.

Keywords Climate networks · El Niño diversity · Ricci-curvature

1 Introduction

The El Niño Southern Oscillation (ENSO) is the largest interannual variation in the global climate system. It is a dynamical atmospheric and oceanic phenomenon characterized by anomalously warm (El Niño) or cold (La Niña) phases of sea surface temperatures (SST) in the equatorial Pacific. Both phases are known to impact earth's climate significantly on long spatial scales, typically referred to as teleconnections (Trenberth, 1997).

*These two authors contributed equally to the paper.

The interrelation between the ‘type’ of El Niño and its impact has been investigated in many studies over the past two decades (Capotondi et al., 2015; Timmermann et al., 2018; Capotondi et al., 2020). The diversity of El Niño events is currently thought to be characterized by two modes: The “canonical” or Eastern Pacific (EP) El Niño with peak SST anomalies in the eastern equatorial Pacific, and the “El Niño Modoki” or Central Pacific (CP) El Niño with peak SST anomalies in the central equatorial Pacific. Although the impact of EP and CP El Niños on different parts of the climate system — such as the Indian Ocean (IO), maritime continent, tropical Atlantic, and Northern America — have been studied thoroughly (see Okumura and Taschetto et al. for an overview), previous work has mainly focused on single teleconnections of the El Niño types. In comparison, little is known about differences in global teleconnection patterns between EP and CP. In this study, we close this gap by presenting a machine learning approach based on the Ricci-curvature of climate networks which detects global teleconnection patterns of the El Niño types and highlights their differences.

Climate networks (Dijkstra et al., 2019) have gained increasing interest for the analysis of spatial dependencies of climatic variables through their ability to reduce data to relevant climatic patterns. They have been widely used in the analysis of ENSO, starting with Tsonis and Swanson, who investigated the topology of El Niño and La Niña networks of surface air temperature. Yamasaki et al. studied the global impact of El Niño on various geographical zones while Donges et al. and Zhou et al. examined geographical long-range teleconnections of ENSO.

Impacts of ENSO diversity have been studied by evolving climate network analyses (Radebach et al., 2013; Kittel et al., 2021). Wiedermann et al. use climate networks to find a robust way to distinguish different types of El Niños and La Niñas. Similarly, Lu et al. use an analysis of climate networks of the Pacific Ocean to distinguish EP and CP events and estimate their expected impacts.

Ricci-curvature measures the deviation of a continuous space from being locally flat and has been recently generalized to discrete spaces like complex networks (Ollivier, 2009; Sreejith et al., 2016). In networks, the Ricci-curvature of a link describes the deviation of its surrounding from a regular grid (each node is connected to its four neighboring nodes). Ricci-curvature highlights whether an edge connects nodes within a community or bridges communities and thereby helps to understand visualize the network structure intuitively, applied for example in the analysis of financial markets (Sandhu et al., 2016), gene expressions (Sandhu et al., 2015; Pouryahya et al., 2018), brain connectivity (Farooq et al., 2019), urban transportation (Gao et al., 2019), power grids (Jonckheere and Grippo, 2019), and epidemiology (de Souza et al., 2021). We use it to reveal global teleconnection patterns and are thereby able to uncover structurally different El Niño impacts.

2 Data and Methods

2.1 Data

We use daily 2-meter air temperature (or surface air temperature, SAT) data for the years 1950–2020 from the ERA5 Global Reanalysis database (Hersbach et al., 2020). We first detrend each time series, then subtract the daily climatology over the whole time period. We use next-neighbor interpolation to map the data to a grid of spatially approximately uniformly distributed points using the Fekete algorithm (Bendito et al., 2007) to avoid spurious correlation patterns close to the poles (Ebert-Uphoff and Deng, 2012). The distance between grid points in the Fekete grid corresponds to 2.5° for points at the equator of a Gaussian grid, resulting in a total of ≈ 6000 grid points.

2.2 Classification of EP and CP El Niño conditions

We classify each day as EP (CP) based on whether the average Dec–Feb SST anomaly in the Niño-3 region is greater (less) than that of the Niño-4 region and Niño-3 (Niño-4) larger than 0.5 (Capotondi et al., 2020). Days that are neither EP, CP, nor La Niña are labeled as ‘normal.’ The SST anomalies are calculated with the Oceanic Niño index baselines, i.e., using multiple centered 30-year base periods, successively updated in 5-year steps. For the end (beginning) of the time period, the last (first) available 30-year base period is used.

2.3 2-meter air temperature Dec–Feb climate networks

Following earlier work on climate networks (Donges et al., 2009a; Wiedermann et al., 2016; Ciemer et al., 2020), we estimate the weighted adjacency matrix \mathbf{W} of the climate network by placing links between pairs of locations which have a correlation value among the 2% strongest absolute correlations. Thus, for the correlation threshold $\rho_{0.98} = Q_{|\rho|}(0.98)$, where $Q_X(\cdot)$ denotes the quantile function for X , we define

$$\mathbf{W}_{ij} = \begin{cases} |\rho_{ij}|, & |\rho_{ij}| > \rho_{0.98} \\ 0, & \text{otherwise} \end{cases}, \quad (1)$$

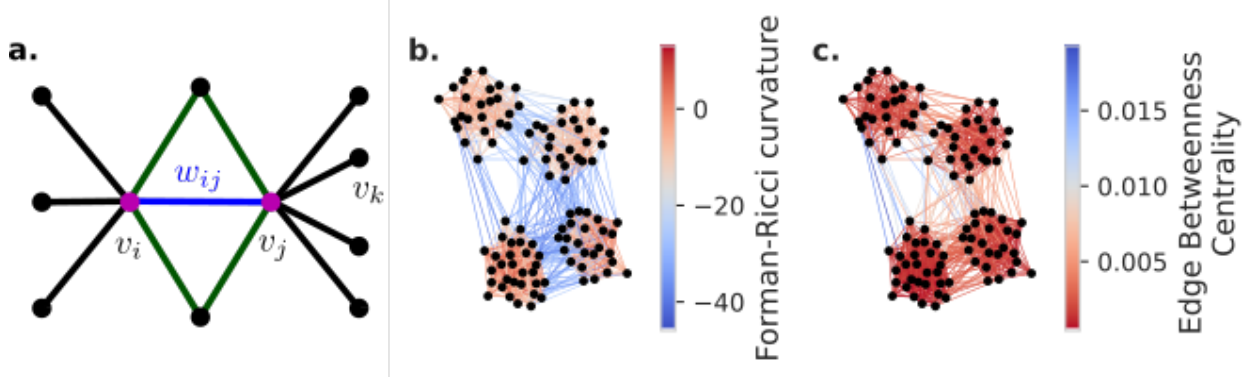


Figure 1: **Curvature of complex networks.** Forman-curvature of an edge with weight w_{ij} connecting nodes v_i and v_j is obtained by Eq. 2 (a). In the synthetic network constructed with a Stochastic Block Model, Forman-curvature (b) provides values to distinguish within-community links (red) from between-community links (blue) in contrast to betweenness centrality (c) with only a few links with high scores. The network with four communities are visualized using the spring layout from NetworkX (Hagberg et al., 2008).

where $i, j \in \{1, \dots, N\}$ index spatial locations and ρ_{ij} is the Dec–Feb Spearman’s rank-order correlation between locations i and j . \mathbf{W}_{ij} thus defines a network $G := (V, E)$ with a set of edges (or links) $e_{ij} \in E$ that connect pairs of nodes $(v_i, v_j) \in V$ with link weight $w_{ij} = |\rho_{ij}|$.

Accounting for autocorrelation in the data, a two-sided test for non-random correlations at a confidence level of 1% yields a threshold $|\hat{\rho}| = 0.35$. While our threshold is far higher, due to the high number of hypotheses tests (3.6×10^7), we nevertheless expect a non-negligible number of network links to be false positives. We thus additionally use a spatial null model which assumes that correlations caused by physical mechanisms are likely part of spatially extended patterns (Boers et al., 2019). For each spatial location, we randomly rewire its network links 2000 times and use a Gaussian kernel density estimator (KDE) to get the likelihood of a link to the chosen location. An observed network link to the chosen location is considered statistically significant if the spatial likelihood of the link (also obtained via Gaussian KDE) is above the 99.9-th percentile of the local null model link distribution.

2.4 Curvature of complex networks

The Ricci-curvature of a network link describes how the connectivity of its network neighborhood differs from the connectivity of a regular grid. Out of two numerical approximations of Ricci curvature on networks — Forman-Ricci curvature (Forman, 2003; Sreejith et al., 2016) and Ollivier-Ricci curvature (Ollivier, 2010) — we use Forman-Ricci curvature (henceforth simply Forman curvature) as it is computationally cheaper and as both definitions are highly correlated, barring slight differences in extreme values (Samal et al., 2018). Forman curvature of edge e_{ij} in an undirected network with weight $w_{ij} \in \mathbf{W}$ is estimated as,

$$F_{ij} = w_{ij} \left(|\mathcal{T}_{ij}| \cdot w_{ij} + \frac{2}{w_{ij}} - \sum_{\substack{k=1 \\ w_{ik}w_{kj}=0}}^N \sum_{\substack{l \in \{i,j\} \\ w_{lk} > 0}} \frac{1}{\sqrt{w_{ij} \cdot w_{lk}}} \right), \quad (2)$$

where $\mathcal{T}_{ij} := \{v_k : w_{ik}w_{jk} > 0\}$ denotes the set of nodes in the neighborhood of v_i and v_j which form triangles containing edge e_{ij} (green edges in Fig. 1a) and $|\cdot|$ denotes set cardinality. The last term in Eq. 2 counts the number of edges adjacent to node v_i and v_j which do not form triangles with edge e_{ij} (black edges in Fig. 1a). Equation 2 approximates the “augmented” Forman curvature (cf. Samal et al., Eq. 9) by considering only triangles, no node weights, and no cycle weights.

Since curvature is in general not symmetrically distributed around zero, we use the 10% most positive curvatures,

$$F_{ij}^+ := \{F_{ij} : F_{ij} > Q_F(0.9)\}, \quad (3)$$

and the 10% most negative curvatures F_{ij}^- (defined similarly as values less than $Q_F(0.1)$). We also define the Forman-curvature of a network node,

$$f_i := \frac{\sum_j F_{ij}}{\sum_j \mathbf{W}_{ij}} \quad (4)$$

to identify geographical locations, or ‘hotspots,’ connected to strongly negatively or positively curved links. As the value ranges of curvature differs for different networks, we use the min-max transform to normalize it to $(-1, 1)$, denoted by \tilde{F}_{ij}^+ . Corresponding to \tilde{F}_{ij}^+ , we use Eq. 4 to define \tilde{f}_i^+ as positive node-curvature hotspots and similarly, \tilde{f}_i^- for negative node-curvature hotspots.

Consider a random network with four communities (Fig. 1 b, c) generated using a stochastic block model from NetworkX (Hagberg et al., 2008). Forman-curvature clearly separates the between-community links from the within-community links. Within-community links are typically part of triangles, indicating local convergence of shortest paths, i.e. positive curvature. Conversely, links connecting nodes with a high degree that are not part of triangles indicate local divergence of shortest paths and negative curvature. Forman-curvature provides a continuous measure over network links that indicates if an edge is inside a community or if it straddles two communities. By comparison, the edge betweenness centrality (see SI sec A)—typically used to identify edges that connect communities— fails to identify many between-community links (Fig. 1c). This is likely due to the binary notion of a shortest path - either a path is the shortest or it is not, implying that “almost-shortest” paths are not considered (SI Eq. 8).

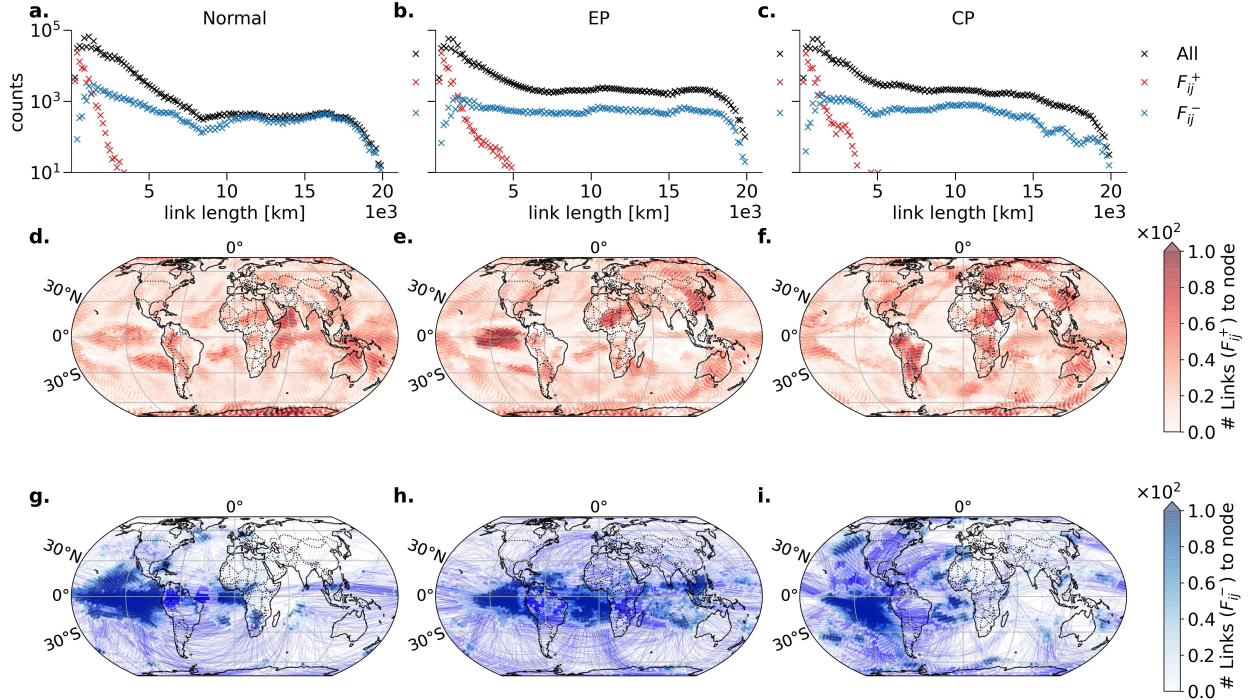


Figure 2: **Forman curvature of normal, EP, and CP El Niño climate network links.** The networks are computed from 2m air temperature anomalies for normal (left column), EP (middle column) and CP (right column) conditions. The first row (a, b, c) depicts the spatial link length distribution for all (black), most positively F_{ij}^+ (red) and most negatively curved F_{ij}^- (blue) edges. The second row (d, e, f) shows F_{ij}^+ , the third row (g, h, i) F_{ij}^- . Colorbars indicate the number of edges to the node. For visual reasons only every 20th edge is plotted in d-i.

3 Results and Discussion

3.1 Spatial organization of teleconnections depends on El Niño type

Fig. 2 a–c shows the distribution of great-circle lengths of the most positively curved F_{ij}^+ and most negatively curved F_{ij}^- network links for normal, EP, and CP conditions respectively. While F_{ij}^- links occur at all spatial scales, F_{ij}^+ links occur only at regional scales less than 5000 km. Long-range teleconnections are thus modulated almost always via negatively curved links; and as the curvature estimation of climate network links does not include any geographical information, likely, the correlation between negative climate network link curvature and long spatial scales is an intrinsic topological property of the SAT dynamics. Furthermore, the spatial distribution of F_{ij}^+ (Fig. 2 d–f) and F_{ij}^- (Fig. 2 g–i) shows that while positive curvature occurs at only regional scales, negative curvature results in link bundles that are related to well-known teleconnection patterns, e.g., the connection between the eastern equatorial Pacific ENSO tongue pattern, and the tropical Atlantic.

The number of most negatively curved links for El Niño conditions does not describe all spatially long-range links, in contrast to normal conditions (Fig. 2 a–c). However, even with the lower number of links, F_{ij}^- links undergo a drastic spatial reorganization for El Niño conditions, especially from normal conditions (Fig. 2 g) to CP conditions (Fig. 2 i). During CP El Niños, e.g., the tropical Pacific shows an enhanced connection to the extratropical Pacific as well as to the mid-latitude North Atlantic region (see Sec. 3.3). Even for EP conditions (Fig. 2 h), we observe that the connection between the tropical Pacific and the southern Atlantic is strengthened in comparison to normal months. Although we find subtle changes in the spatial organization of the most positively curved links between normal (Fig. 2 d) and El Niño conditions (Fig. 2 e, f), such as weakening of regional correlation structures in the tropical Atlantic and strengthening of correlation in the West African monsoon belt, these changes are not as drastic as the ones that occur in the negatively curved links.

Note, we mainly discover teleconnections within the global oceans because correlations are generally higher over oceans than over land due to slower oceanic SAT variability (Lambert et al., 2011).

3.2 EP El Niño teleconnections are tropical, while CP El Niño teleconnections are at all latitudes

Positive curvature hotspots, \tilde{f}_i^+ , for EP conditions reveal the well-known ENSO tongue (Fig. 3b) typically observed in empirical orthogonal function analysis of sea surface temperature data (Johnson, 2013). We also find pronounced regions of \tilde{f}_i^+ in the IO and tropical Atlantic, which are known to be affected by strong EP El Niño events (Klein et al., 1999; Zhang et al., 2015; Rodrigues et al., 2015). Under CP conditions, \tilde{f}_i^+ is spread over all latitudes and over different regions of the globe (Fig. 3c). For instance, we observe a hotspot in the tropical Pacific similar to the El Niño tongue, which is however shifted towards the dateline and also extended southwards. The spatial pattern under CP conditions is more similar to normal months (Fig. 3a) than under EP conditions. \tilde{f}_i^+ shows strong similarity to node degree (SI 6).

Negative node-curvature hotspots, \tilde{f}_i^- , for EP conditions (Fig. 3e) show enhanced teleconnections arising from South China Sea, tropical IO, eastern tropical Pacific, and the tropical Atlantic. This coincides with a decrease in teleconnections arising from the extratropical Pacific, southern IO, North Atlantic (near Greenland), and the Southern Ocean. As with \tilde{f}_i^+ , here too the spatial pattern of CP conditions (Fig. 3f) is spread all over the globe and looks more similar to normal conditions (Fig. 3d), barring the northern tropical Pacific and the North Atlantic, both of which show a decrease in teleconnections.

Overall, EP conditions result in confinement of hotspots around the tropics for both regional links and teleconnections, which is further confirmed by comparing the zonal medians shown in Fig. 3 g–i. CP conditions, on the other hand, show only minor differences from normal months, although the magnitude of curvature values increase (SI 9). This partly corroborates previous work (Wiedermann et al., 2016; Lu et al., 2020) which also reports a strong localization of climate network links during EP conditions. These studies, however, did not focus on the impact of ENSO diversity on climate network teleconnections.

3.3 EP and CP El Niño teleconnection patterns of eastern and central Pacific Ocean, IO, and Labrador Sea

Teleconnections link the Niño 3 region (Fig. 4a) to the tropical Atlantic during both EP and CP conditions, supporting earlier work showing that strong El Niños can lead to warming in the tropical Atlantic mediated by the tropospheric temperature mechanism (Chang et al., 2006) and the atmospheric bridge via the Pacific North Atlantic (PNA) pattern (Rodrigues et al., 2011). There are also links from the Niño 3 region that appear only under EP conditions, such as those that connect to the IO, likely arising because of the influence of eastern tropical Pacific SSTs on the IO during and after El Niño events (Klein et al., 1999). Some links from the Niño 3 box arise only under CP conditions, primarily

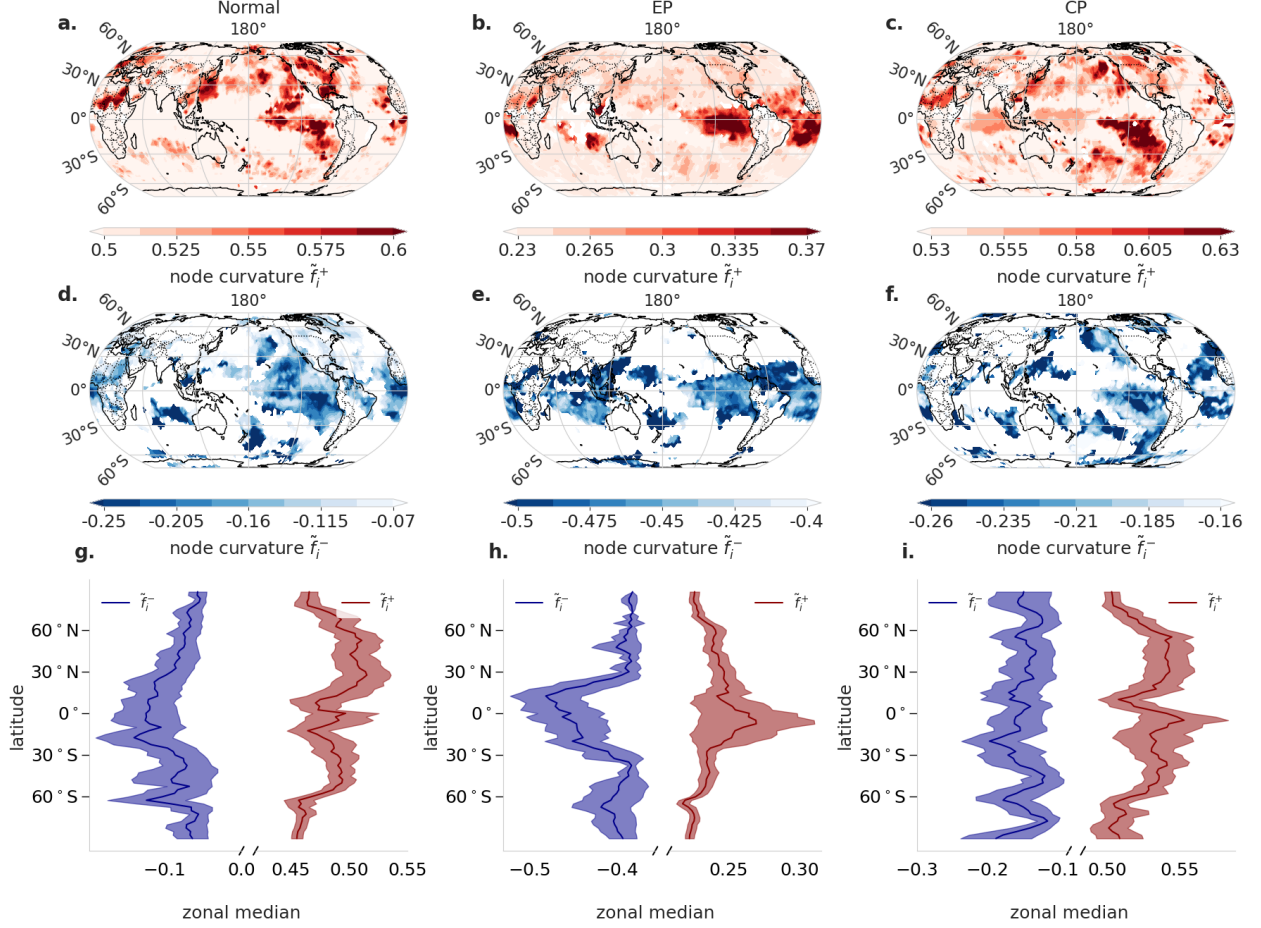


Figure 3: **Node curvature of normal, EP El Niño, and CP El Niño climate networks.** Node curvature for most positively curved, \tilde{f}_i^+ (a-c) and most negatively curved, \tilde{f}_i^- (d-f) links are shown. EP hotspots (middle column) are more constrained to the tropics than for CP (right column). $\tilde{f}_i^{+/-}$ for normal conditions (left column) shows more similarity to CP than to EP. Zonal medians of \tilde{f}_i^+ (red) and \tilde{f}_i^- (blue) further confirm this similarity. (g-i).

connecting the extratropical Pacific. These links are likely due to the North and South Pacific Meridional Mode (NPMM and SPMM), as atmospheric and oceanic anomalies in the extratropics associated with SPMM and NPMM affect the intensity and flavor of El Niño (You and Furtado, 2018). The relationship of NPMM and SPMM with ENSO diversity is, however, still under debate (Amaya, 2019).

The teleconnections of the Niño 4 region (Fig. 4b) are far fewer compared to the Niño 3 region (Fig. 4a). It is rather surprising that the Niño 4 region is not well connected even during CP conditions, although a CP El Niño is primarily characterised by higher SST anomalies in the Niño 4 region than in the Niño 3 region. A likely explanation is that although the temperature fields are more anomalous in the central Pacific during CP conditions, the impacts of these anomalies are nevertheless mediated via the eastern Pacific. We find the same result for climate networks created from networks with shorter time ranges as well.

The IO has a large number of most negatively curved links during EP conditions but not for CP (Fig. 3 c, d). The EP event teleconnections link the IO to the tropical Atlantic and Pacific basin (Fig. 4 c). The links to the tropical Atlantic could be either attributed to indirect links mitigated by the impact of the Niño 3 region to the tropical Atlantic or might resemble direct impact between the oceans as recently described by Zhang and Han. CP conditions do not result in teleconnections in the IO as CP events are generally weaker (Zhang et al., 2015).

The Labrador Sea (Fig. 4d) is another pronounced area of most negative node-curvature in the CP network not present in the EP network (compare Fig. 3 c,d). Edges with the most negative curvature adjacent to the Labrador Sea connect to

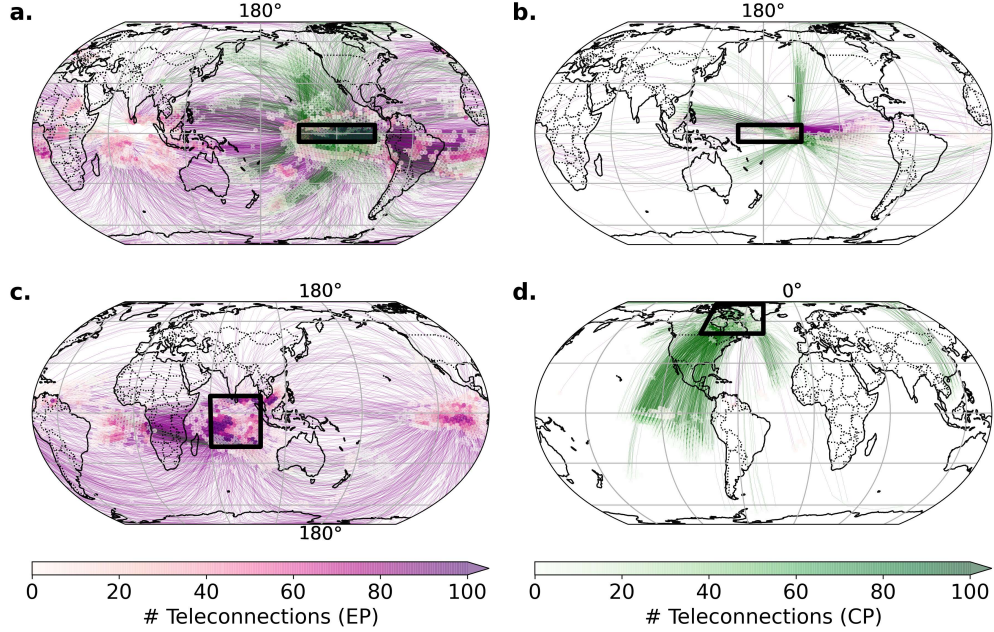


Figure 4: **Teleconnections arising from eastern and central Pacific Ocean, IO, and Labrador Sea.** F_{ij}^- , i.e. teleconnections, for EP (purple) and CP (green) El Niño events connected to the four selected regions (black rectangles): Niño 3 (a), Niño 4 (b), IO (c), and Labrador Sea (d). For visual clarity, only a third of all links are shown.

the eastern tropical Pacific and the extra tropical Atlantic. This pattern may be attributed to the North Atlantic Oscillation (NAO), which refers to sea level pressure changes in the Arctic and subtropical Atlantic (Jiménez-Estevé and Domeisen, 2018). El Niño is known to cause a negative NAO pattern driven by the PNA pattern where a negative NAO phase is attributable to CP El Niño events via the subtropical bridge (Graf and Zanchettin, 2012; Domeisen et al., 2019).

Regressing the SAT fields against the data in the four boxes corroborates the findings from the curvature-based analysis (Fig. 5, SI Fig. 11, 12, 13). The Niño 3 region is highly teleconnected during both EP and CP conditions, but the spatial organization is different between the two (Fig. 5 a, b). The tropical Indian and Atlantic oceans are well modeled during EP and the tropical-extratropical links in the Pacific and the Labrador Sea are well modeled during CP. By contrast, the Niño 4 box explains very little of the temperature fields irrespective of the El Niño type (Fig. 5 c, d). Similarly, we find that the IO is highly active during EP but not during CP conditions (Fig. 5 e, f); and that the Labrador Sea is correlated to the tropics only during CP (Fig. 5 g, i). Note that we can identify the teleconnection patterns only because we have the results from the curvature-based climate network analysis to guide our interpretations of the correlation maps. Without the curvature analysis, i.e. using simple correlation maps (SI Fig. 10) or classical complex network measures (SI Fig. 6, 7, 8), it is not trivial to figure out the most important regions for each El Niño flavor.

4 Conclusion

We presented a new approach to estimate global teleconnection patterns of 2-meter air temperature and used it to investigate the teleconnections of Eastern Pacific and Central Pacific El Niño events. Our approach involves correlation-based climate networks and a recently established network measure based on Ricci-curvature. In particular, we used Forman-Ricci curvature to distinguish links related to small-scale regional structures (positively curved links) from long-range teleconnections connecting regions from different parts of the globe (negatively curved links).

We showed that El Niños diversity drastically impacts the spatial organization of teleconnections. Using node-based curvature, we identified teleconnection hotspots for both EP and CP conditions. Our results showed that teleconnections in the EP climate network were mainly confined to the tropics, whereas CP network teleconnections were found at northern and southern mid-latitudes as well. We further investigated the impact of ENSO diversity on the teleconnection patterns of four specific regions: the Niño 3 region, the Niño 4 region, the northern IO, and the Labrador Sea. We found that the Niño 3 region in the eastern Pacific has a large number of teleconnections irrespective of whether we consider EP or CP conditions, whereas the Niño 4 region in the central Pacific has, by comparison, very few teleconnections under both EP and CP conditions. We thus conclude that the eastern Pacific is the primary mediator of El Niño impacts

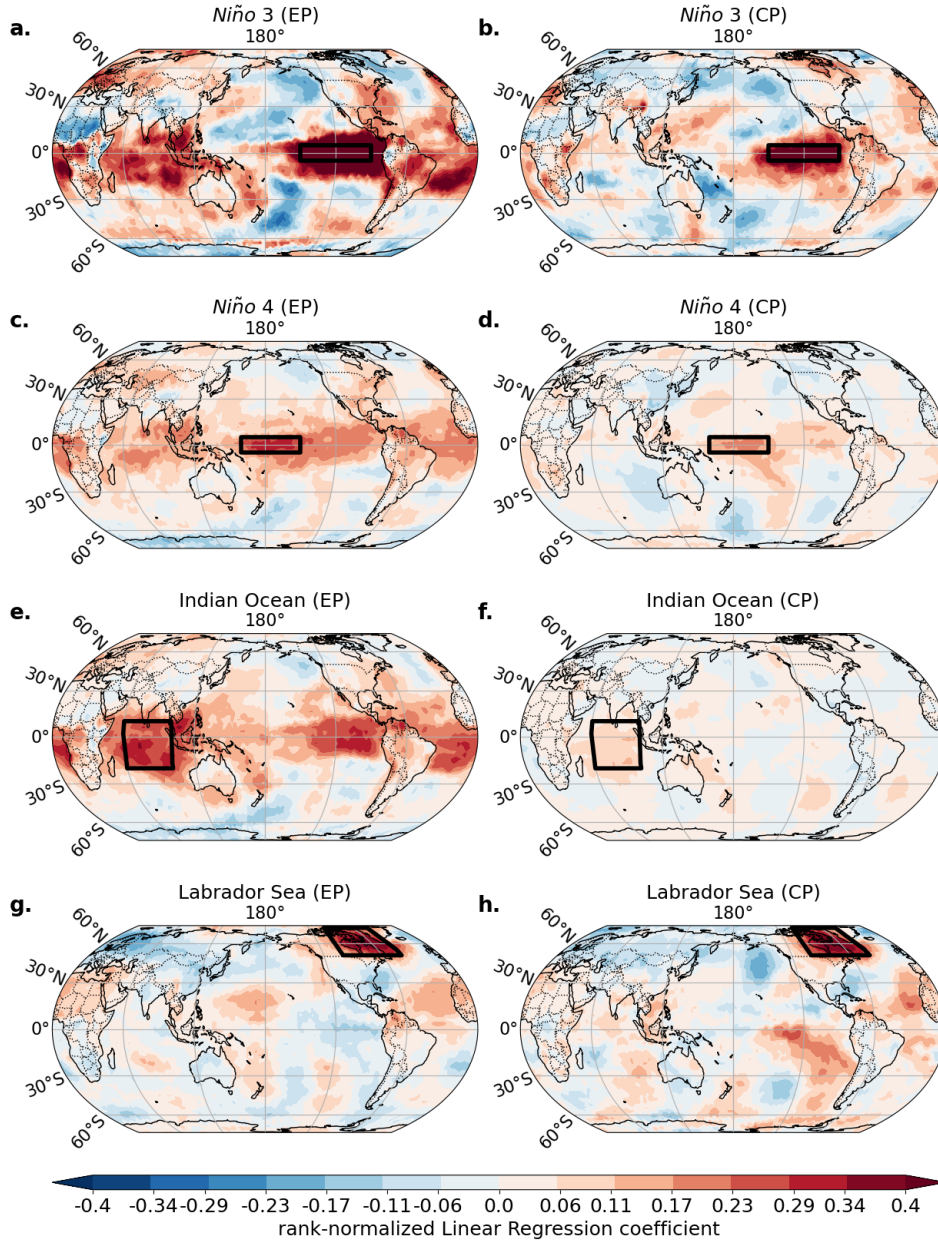


Figure 5: **SAT fields regressed on temperatures from the four selected regions.** Rank-normalized SAT time series at each location is regressed against all the rank-normalized SAT time series inside the four regions (black rectangles, same as in Fig. 4) for EP events (left column) and CP events (right column) and the average linear regression coefficient is shown.

irrespective of the El Niño type, and acknowledge that further work on the role of the eastern Pacific during CP El Niños is needed. We found that the northern IO and the Labrador Sea show teleconnections almost only under EP and CP conditions respectively. While the teleconnections of the IO region to the Niño 3 region during EP conditions are well-known, the links between the Labrador Sea to the eastern tropical Pacific and northern tropical Atlantic are not fully understood.

Open Research

Datasets for this research are available from Copernicus Climate Change Service. The data from 1979 till date was taken from Hersbach et al. and the data from 1950 to 1979 from Bell et al.. The code for generating and analyzing the networks is made publicly available under Strnad and Schlör. The code for reproducing the analysis of the network curvature described in this paper is publicly available under Schlör and Strnad.

Acknowledgment

Funded by the Deutsche Forschungsgemeinschaft (DFG, German Research Foundation) under Germany’s Excellence Strategy – EXC number 2064/1 – Project number 390727645. The authors thank the International Max Planck Research School for Intelligent Systems (IMPRS-IS) for supporting Jakob Schlör and Felix Strnad.

References

- D. J. Amaya. The Pacific Meridional Mode and ENSO: a Review. *Curr. Clim. Change Rep.*, 5(4):296–307, Dec 2019. ISSN 2198-6061. doi:10.1007/s40641-019-00142-x.
- B. Bell, H. Hersbach, P. Berrisford, P. Dahlgren, A. Horányi, J. Muñoz Sabater, J. Nicolas, R. Radu, D. Schepers, A. Simmons, C. Soci, and J.-N. Thépaut. Era5 hourly data on single levels from 1950 to 1978 (preliminary version), 2020. URL <https://cds.climate.copernicus-climate.eu/cdsapp#!/dataset/reanalysis-era5-single-levels-preliminary-back-extension>. Accessed on 02-03-2022.
- E. Bendito, A. Carmona, A. M. Encinas, and J. M. Gesto. Estimation of Fekete points. *J. Comput. Phys.*, 225(2): 2354–2376, Aug 2007. ISSN 0021-9991. doi:10.1016/j.jcp.2007.03.017.
- N. Boers, B. Bookhagen, N. Marwan, J. Kurths, and J. Marengo. Complex networks identify spatial patterns of extreme rainfall events of the South American Monsoon System. *Geophys. Res. Lett.*, 40(16):4386–4392, Aug 2013. ISSN 0094-8276. doi:10.1002/grl.50681.
- N. Boers, B. Goswami, A. Rheinwalt, B. Bookhagen, B. Hoskins, and J. Kurths. Complex networks reveal global pattern of extreme-rainfall teleconnections. *Nature*, 566(7744):373–377, 2019. ISSN 14764687. doi:10.1038/s41586-018-0872-x. URL <http://dx.doi.org/10.1038/s41586-018-0872-x>.
- A. Capotondi, A. T. Wittenberg, M. Newman, E. Di Lorenzo, J.-Y. Yu, P. Braconnot, J. Cole, B. Dewitte, B. Giese, E. Guilyardi, F.-F. Jin, K. Karnauskas, B. Kirtman, T. Lee, N. Schneider, Y. Xue, and S.-W. Yeh. Understanding ENSO Diversity. *Bull. Am. Meteorol. Soc.*, 96(6):921–938, Jun 2015. ISSN 0003-0007. doi:10.1175/BAMS-D-13-00117.1.
- A. Capotondi, A. T. Wittenberg, J.-S. Kug, K. Takahashi, and M. J. McPhaden. ENSO Diversity. In *El Niño Southern Oscillation in a Changing Climate*, pages 65–86. American Geophysical Union (AGU), Nov 2020. ISBN 978-1-11954816-4. doi:10.1002/9781119548164.ch4.
- P. Chang, Y. Fang, R. Saravanan, L. Ji, and H. Seidel. The cause of the fragile relationship between the Pacific El Niño and the Atlantic Niño. *Nature*, 443:324–328, Sep 2006. ISSN 1476-4687. doi:10.1038/nature05053.
- C. Ciemer, N. Boers, H. M. J. Barbosa, J. Kurths, and A. Rammig. Temporal evolution of the spatial covariability of rainfall in South America. *Clim. Dyn.*, 51(1):371–382, Jul 2018. ISSN 1432-0894. doi:10.1007/s00382-017-3929-x.
- C. Ciemer, L. Rehm, J. Kurths, R. V. Donner, R. Winkelmann, and N. Boers. An early-warning indicator for Amazon droughts exclusively based on tropical Atlantic sea surface temperatures. *Environ. Res. Lett.*, 15(9):094087, Sep 2020. ISSN 1748-9326. doi:10.1088/1748-9326/ab9cff.
- D. B. de Souza, J. T. S. da Cunha, E. F. dos Santos, J. B. Correia, H. P. da Silva, J. L. de Lima Filho, J. Albuquerque, and F. A. N. Santos. Using discrete Ricci curvatures to infer COVID-19 epidemic network fragility and systemic risk. *J. Stat. Mech.: Theory Exp.*, 2021(5):053501, May 2021. ISSN 1742-5468. doi:10.1088/1742-5468/abed4e.
- H. A. Dijkstra, E. Hernández-García, C. Masoller, and M. Barreiro. *Networks in Climate*. Cambridge University Press, Cambridge, England, UK, Feb 2019. ISBN 978-1-31627575-7. doi:10.1017/9781316275757.

- D. I. V. Domeisen, C. I. Garfinkel, and A. H. Butler. The Teleconnection of El Niño Southern Oscillation to the Stratosphere. *Rev. Geophys.*, 57(1):5–47, Mar 2019. ISSN 8755-1209. doi:10.1029/2018RG000596.
- J. F. Donges, Y. Zou, N. Marwan, and J. Kurths. The backbone of the climate network. *EPL (Europhysics Letters)*, 87(4):48007, sep 2009a. ISSN 0295-5075. doi:10.1209/0295-5075/87/48007.
- J. F. Donges, Y. Zou, N. Marwan, and J. Kurths. Complex networks in climate dynamics. *The European Physical Journal Special Topics*, 174(1):157–179, 2009b.
- J. F. Donges, I. Petrova, A. Loew, N. Marwan, and J. Kurths. How complex climate networks complement eigen techniques for the statistical analysis of climatological data. *Clim. Dyn.*, 45(9):2407–2424, Nov 2015. ISSN 1432-0894. doi:10.1007/s00382-015-2479-3.
- I. Ebert-Uphoff and Y. Deng. A new type of climate network based on probabilistic graphical models: Results of boreal winter versus summer. *Geophysical Research Letters*, 39(18):1–7, 2012. ISSN 00948276. doi:10.1029/2012GL053269.
- H. Farooq, Y. Chen, T. T. Georgiou, A. Tannenbaum, and C. Lenglet. Network curvature as a hallmark of brain structural connectivity - Nature Communications. *Nat. Commun.*, 10(4937):1–11, Oct 2019. ISSN 2041-1723. doi:10.1038/s41467-019-12915-x.
- R. Forman. Bochner’s method for cell complexes and combinatorial Ricci curvature. *Discrete and Computational Geometry*, 29(3):323–374, 2003.
- L. C. Freeman. A Set of Measures of Centrality Based on Betweenness. *Sociometry*, 40(1):35–41, 1977. URL <https://www.jstor.org/stable/3033543>.
- L. Gao, X. Liu, Y. Liu, P. Wang, M. Deng, Q. Zhu, and H. Li. Measuring road network topology vulnerability by Ricci curvature. *Physica A*, 527:121071, Aug 2019. ISSN 0378-4371. doi:10.1016/j.physa.2019.121071.
- H.-F. Graf and D. Zanchettin. Central Pacific El Niño, the “subtropical bridge,” and Eurasian climate. *J. Geophys. Res. Atmos.*, 117(D1), Jan 2012. ISSN 0148-0227. doi:10.1029/2011JD016493.
- A. A. Hagberg, D. A. Schult, and P. J. Swart. Exploring network structure, dynamics, and function using networkx. In G. Varoquaux, T. Vaught, and J. Millman, editors, *Proceedings of the 7th Python in Science Conference*, pages 11 – 15, Pasadena, CA USA, 2008. URL http://conference.scipy.org/proceedings/SciPy2008/paper_2.
- H. Hersbach, B. Bell, P. Berrisford, G. Biavati, A. Horányi, J. Muñoz Sabater, J. Nicolas, C. Peubey, R. Radu, I. Rozum, D. Schepers, A. Simmons, C. Soci, D. Dee, and J.-N. Thépaut. Era5 hourly data on single levels from 1979 to present, 2018. Accessed on 02-03-2022.
- H. Hersbach, B. Bell, P. Berrisford, S. Hirahara, A. Horányi, J. Muñoz-Sabater, J. Nicolas, C. Peubey, R. Radu, D. Schepers, A. Simmons, C. Soci, S. Abdalla, X. Abellan, G. Balsamo, P. Bechtold, G. Biavati, J. Bidlot, M. Bonavita, G. De Chiara, P. Dahlgren, D. Dee, M. Diamantakis, R. Dragani, J. Flemming, R. Forbes, M. Fuentes, A. Geer, L. Haimberger, S. Healy, R. J. Hogan, E. Hólm, M. Janisková, S. Keeley, P. Laloyaux, P. Lopez, C. Lupu, G. Radnoti, P. de Rosnay, I. Rozum, F. Vamborg, S. Villaume, and J. N. Thépaut. The ERA5 global reanalysis. *Quarterly Journal of the Royal Meteorological Society*, 146(730):1999–2049, 2020. ISSN 1477870X. doi:10.1002/qj.3803.
- B. Jiménez-Esteve and D. I. V. Domeisen. The Tropospheric Pathway of the ENSO–North Atlantic Teleconnection. *J. Clim.*, 31(11):4563–4584, Jun 2018. ISSN 0894-8755. doi:10.1175/JCLI-D-17-0716.1.
- N. C. Johnson. How Many ENSO Flavors Can We Distinguish? *J. Clim.*, 26(13):4816–4827, Jul 2013. ISSN 0894-8755. doi:10.1175/JCLI-D-12-00649.1.
- E. Jonckheere and E. Grippo. Ollivier-Ricci Curvature Approach to Cost-Effective Power Grid Congestion Management. In *2019 Chinese Control And Decision Conference (CCDC)*, pages 2118–2123. IEEE, Jun 2019. doi:10.1109/CCDC.2019.8832819.
- T. Kittel, C. Ciemer, N. Lotfi, T. Peron, F. Rodrigues, J. Kurths, and R. V. Donner. Evolving climate network perspectives on global surface air temperature effects of ENSO and strong volcanic eruptions. *Eur. Phys. J. Spec. Top.*, 230(14):3075–3100, Oct 2021. ISSN 1951-6401. doi:10.1140/epjs/s11734-021-00269-9.
- S. A. Klein, B. J. Soden, and N.-C. Lau. Remote Sea Surface Temperature Variations during ENSO: Evidence for a Tropical Atmospheric Bridge. *J. Clim.*, 12(4):917–932, Apr 1999. ISSN 0894-8755. doi:10.1175/1520-0442(1999)012<0917:RSSTVD>2.0.CO;2.
- F. H. Lambert, M. J. Webb, and M. M. Joshi. The Relationship between Land–Ocean Surface Temperature Contrast and Radiative Forcing. *J. Clim.*, 24(13):3239–3256, Jul 2011. ISSN 0894-8755. doi:10.1175/2011JCLI3893.1.
- Z. Lu, N. Yuan, L. Chen, and Z. Gong. On the Impacts of El Niño Events: A New Monitoring Approach Using Complex Network Analysis. *Geophys. Res. Lett.*, 47(6):e2019GL086533, Mar 2020. ISSN 0094-8276. doi:10.1029/2019GL086533.

- Y. M. Okumura. ENSO Diversity from an Atmospheric Perspective. *Curr. Clim. Change Rep.*, 5(3):245–257, Sep 2019. ISSN 2198-6061. doi:10.1007/s40641-019-00138-7.
- Y. Ollivier. Ricci curvature of markov chains on metric spaces. *Journal of Functional Analysis*, 256(3):810–864, 2009.
- Y. Ollivier. A survey of Ricci curvature for metric spaces and markov chains. In *Probabilistic approach to geometry*, pages 343–381. Mathematical Society of Japan, 2010.
- M. Pouryahya, J. H. Oh, J. C. Mathews, J. O. Deasy, and A. R. Tannenbaum. Characterizing Cancer Drug Response and Biological Correlates: A Geometric Network Approach - Scientific Reports. *Sci. Rep.*, 8(6402):1–12, Apr 2018. ISSN 2045-2322. doi:10.1038/s41598-018-24679-3.
- A. Radebach, R. V. Donner, J. Runge, J. F. Donges, and J. Kurths. Disentangling different types of El Niño episodes by evolving climate network analysis. *Phys. Rev. E*, 88(5):052807, Nov 2013. ISSN 2470-0053. doi:10.1103/PhysRevE.88.052807.
- R. R. Rodrigues, R. J. Haarsma, E. J. D. Campos, and T. Ambrizzi. The Impacts of Inter-El Niño Variability on the Tropical Atlantic and Northeast Brazil Climate. *J. Clim.*, 24(13):3402–3422, Jul 2011. ISSN 0894-8755. doi:10.1175/2011JCLI3983.1.
- R. R. Rodrigues, E. J. D. Campos, and R. Haarsma. The Impact of ENSO on the South Atlantic Subtropical Dipole Mode. *J. Clim.*, 28(7):2691–2705, Apr 2015. ISSN 0894-8755. doi:10.1175/JCLI-D-14-00483.1.
- A. Samal, R. P. Sreejith, J. Gu, S. Liu, E. Saucan, and J. Jost. Comparative analysis of two discretizations of Ricci curvature for complex networks - Scientific Reports. *Sci. Rep.*, 8(8650):1–16, Jun 2018. ISSN 2045-2322. doi:10.1038/s41598-018-27001-3.
- R. Sandhu, T. Georgiou, E. Reznik, L. Zhu, I. Kolesov, Y. Senbabaoglu, and A. Tannenbaum. Graph Curvature for Differentiating Cancer Networks - Scientific Reports. *Sci. Rep.*, 5(12323):1–13, Jul 2015. ISSN 2045-2322. doi:10.1038/srep12323.
- R. S. Sandhu, T. T. Georgiou, and A. R. Tannenbaum. Ricci curvature: An economic indicator for market fragility and systemic risk. *Sci. Adv.*, May 2016. URL <https://www.science.org/doi/10.1126/sciadv.1501495#F2>.
- J. Schlör and F. Strnad. netcurvature. *Zenodo*, v1.0.0, 2022. doi:<https://doi.org/10.5281/zenodo.6325299>.
- R. Sreejith, K. Mohanraj, J. Jost, E. Saucan, and A. Samal. Forman curvature for complex networks. *Journal of Statistical Mechanics: Theory and Experiment*, 2016(6):063206, 2016.
- F. Strnad and J. Schlör. climnet. *Zenodo*, v1.0.0, 2022. doi:<https://doi.org/10.5281/zenodo.6325661>.
- A. S. Taschetto, C. C. Ummenhofer, M. F. Stuecker, D. Dommenges, K. Ashok, R. R. Rodrigues, and S.-W. Yeh. ENSO Atmospheric Teleconnections. In *El Niño Southern Oscillation in a Changing Climate*, pages 309–335. American Geophysical Union (AGU), Nov 2020. ISBN 978-1-11954816-4. doi:10.1002/9781119548164.ch14.
- A. Timmermann, S.-I. An, J.-S. Kug, F.-F. Jin, W. Cai, A. Capotondi, K. M. Cobb, M. Lengaigne, M. J. McPhaden, M. F. Stuecker, K. Stein, A. T. Wittenberg, K.-S. Yun, T. Bayr, H.-C. Chen, Y. Chikamoto, B. Dewitte, D. Dommenges, P. Grothe, E. Guilyardi, Y.-G. Ham, M. Hayashi, S. Ineson, D. Kang, S. Kim, W. Kim, J.-Y. Lee, T. Li, J.-J. Luo, S. McGregor, Y. Planton, S. Power, H. Rashid, H.-L. Ren, A. Santoso, K. Takahashi, A. Todd, G. Wang, G. Wang, R. Xie, W.-H. Yang, S.-W. Yeh, J. Yoon, E. Zeller, and X. Zhang. El Niño–Southern Oscillation complexity - *Nature*. *Nature*, 559:535–545, Jul 2018. ISSN 1476-4687. doi:10.1038/s41586-018-0252-6.
- K. E. Trenberth. The Definition of El Niño. *Bull. Am. Meteorol. Soc.*, 78(12):2771–2778, 1997. ISSN 0003-0007. doi:10.1175/1520-0477(1997)078<2771:TDOENO>2.0.CO;2.
- A. A. Tsonis and K. L. Swanson. Topology and Predictability of El Niño and La Niña Networks. *Phys. Rev. Lett.*, 100(22):228502, Jun 2008. ISSN 1079-7114. doi:10.1103/PhysRevLett.100.228502.
- M. Wiedermann, A. Radebach, J. F. Donges, J. Kurths, and R. V. Donner. A climate network-based index to discriminate different types of El Niño and La Niña. *Geophys. Res. Lett.*, 43(13):7176–7185, Jul 2016. ISSN 0094-8276. doi:10.1002/2016GL069119.
- K. Yamasaki, A. Gozolchiani, and S. Havlin. Climate Networks around the Globe are Significantly Affected by El Niño. *Phys. Rev. Lett.*, 100(22):228501, Jun 2008. ISSN 1079-7114. doi:10.1103/PhysRevLett.100.228501.
- Y. You and J. C. Furtado. The South Pacific Meridional Mode and Its Role in Tropical Pacific Climate Variability. *J. Clim.*, 31(24):10141–10163, Dec 2018. ISSN 0894-8755. doi:10.1175/JCLI-D-17-0860.1.
- L. Zhang and W. Han. Indian Ocean Dipole leads to Atlantic Niño - *Nature Communications*. *Nat. Commun.*, 12(5952):1–9, Oct 2021. ISSN 2041-1723. doi:10.1038/s41467-021-26223-w.
- W. Zhang, Y. Wang, F.-F. Jin, M. F. Stuecker, and A. G. Turner. Impact of different El Niño types on the El Niño/IOD relationship. *Geophys. Res. Lett.*, 42(20):8570–8576, Oct 2015. ISSN 0094-8276. doi:10.1002/2015GL065703.

D. Zhou, A. Gozolchiani, Y. Ashkenazy, and S. Havlin. Teleconnection Paths via Climate Network Direct Link Detection. *Phys. Rev. Lett.*, 115(26):268501, Dec 2015. ISSN 1079-7114. doi:10.1103/PhysRevLett.115.268501.

Supplementary Information

A Complex Network Measures

Assume complex network graph G , defined by its set of nodes V , connected by its set of edges E , where e_{ij} denotes an edge connecting node v_i to node v_j . This type of a graph is described by its adjacency matrix \mathbf{A} :

$$\mathbf{A}_{ij} = \begin{cases} 1, & e_{ij} \in E \\ 0, & \text{otherwise} \end{cases},$$

If the edges e_{ij} are weighted by weights w_{ij} , the weighted graph is described by

$$\mathbf{W}_{ij} = \begin{cases} w_{ij}, & e_{ij} \in E \\ 0, & \text{otherwise} \end{cases},$$

Node degree The node degree \tilde{k}_i and the weighted node degree k_i is a frequently applied measure to study complex networks (Donges et al., 2009b; Boers et al., 2013; Donges et al., 2015). It counts the (weighted) number of neighboring nodes to node v_i , defined by:

$$k_i = \sum_j^N \mathbf{W}_{ij}, \quad (5)$$

$$\tilde{k}_i = \sum_j^N \mathbf{A}_{ij}, \quad (6)$$

where N denotes the number of nodes $v_i \in V$.

In Figure 6 the node degree is visualized for normal (6 **a**), EP (6 **b**) and CP (6 **c**) networks.

Betweenness Centrality Betweenness Centrality is defined for nodes v and edges e as,

$$BC_v(v_i) = \sum_{s,t}^N \frac{\sigma(v_s, v_t | v_i)}{\sigma(v_s, v_t)}, \quad (7)$$

$$BC_e(e_{ij}) = \sum_{s,t}^N \frac{\sigma(v_s, v_t | e_{ij})}{\sigma(v_s, v_t)}, \quad (8)$$

where $\sigma(v_s, v_t)$ denotes the number of shortest paths between nodes v_s and v_t and $\sigma(v_s, v_t | v_i) \leq \sigma(v_s, v_t)$ the number of all shortest paths that include node v_i . Similarly for edge betweenness centrality $\sigma(v_s, v_t | e_{ij}) \leq \sigma(v_s, v_t)$ yields the number of all shortest paths that include edge e_{ij} . For instance, betweenness centrality measures were used in (Freeman, 1977; Donges et al., 2009a; Boers et al., 2013; Ciemer et al., 2018). BC_n is often referred to as pathway of a variable through the network and therefore taken as an indicator for the flow of the variable of interest. In Figure 7 the node degree is visualized for normal year (7 **a**), EP (7 **b**) and CP (7 **c**) conditions.

Clustering Coefficient The clustering coefficient of a node v_i is defined by the fraction of possible triangles through the actual number of nodes in the network normalized by the unweighted node degree \tilde{k}_i :

$$c_i = \frac{2\mathcal{T}(v_i)}{\tilde{k}_i(\tilde{k}_i - 1)}. \quad (9)$$

Here, $\mathcal{T}(v_i)$ describes the number of triangles including node v_i .

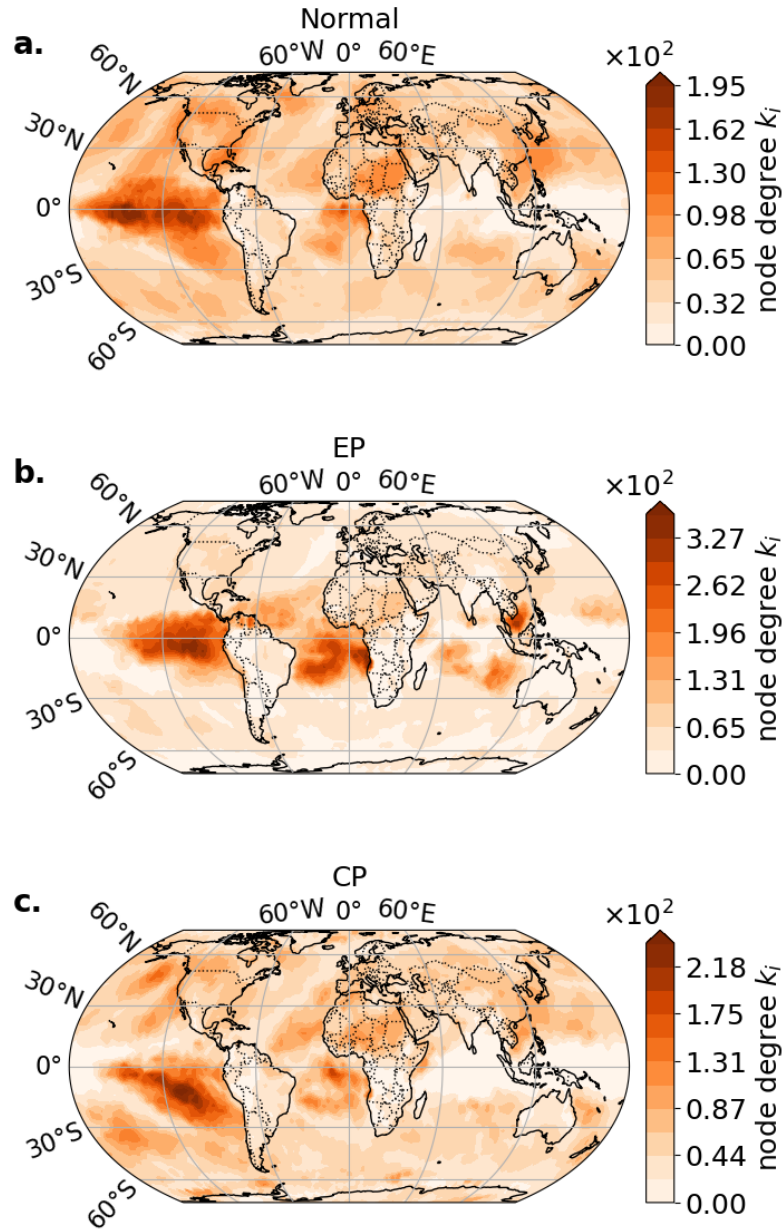


Figure 6: **Node degree for normal, EP and CP conditions.** The weighted node degree is computed following Eq. 5. The climate networks are obtained for normal (a), on Eastern Pacific El Niño (b) and on Central Pacific El Niño (c) conditions.

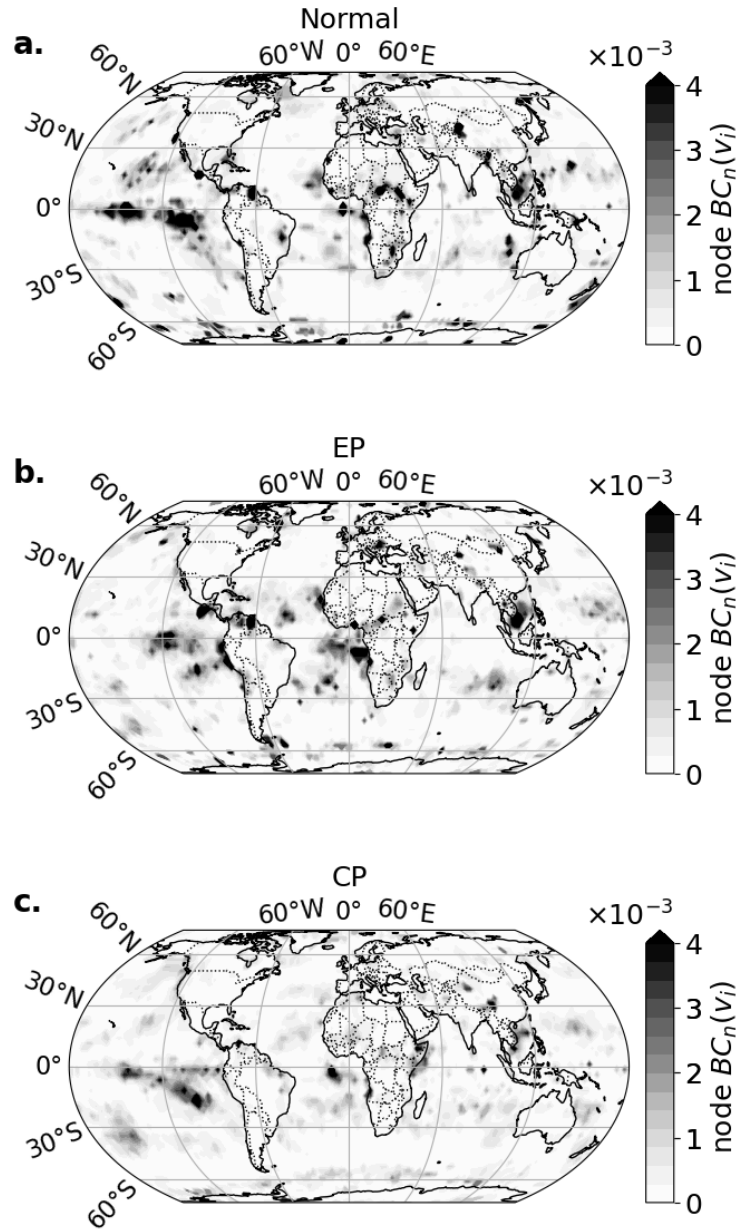


Figure 7: **Node Betweenness Centrality for normal, EP and CP conditions.** The betweenness centrality is computed using Eq. 7. The climate networks obtained for normal (a), on Eastern Pacific El Niño (b) and on Central Pacific El Niño (c) conditions.

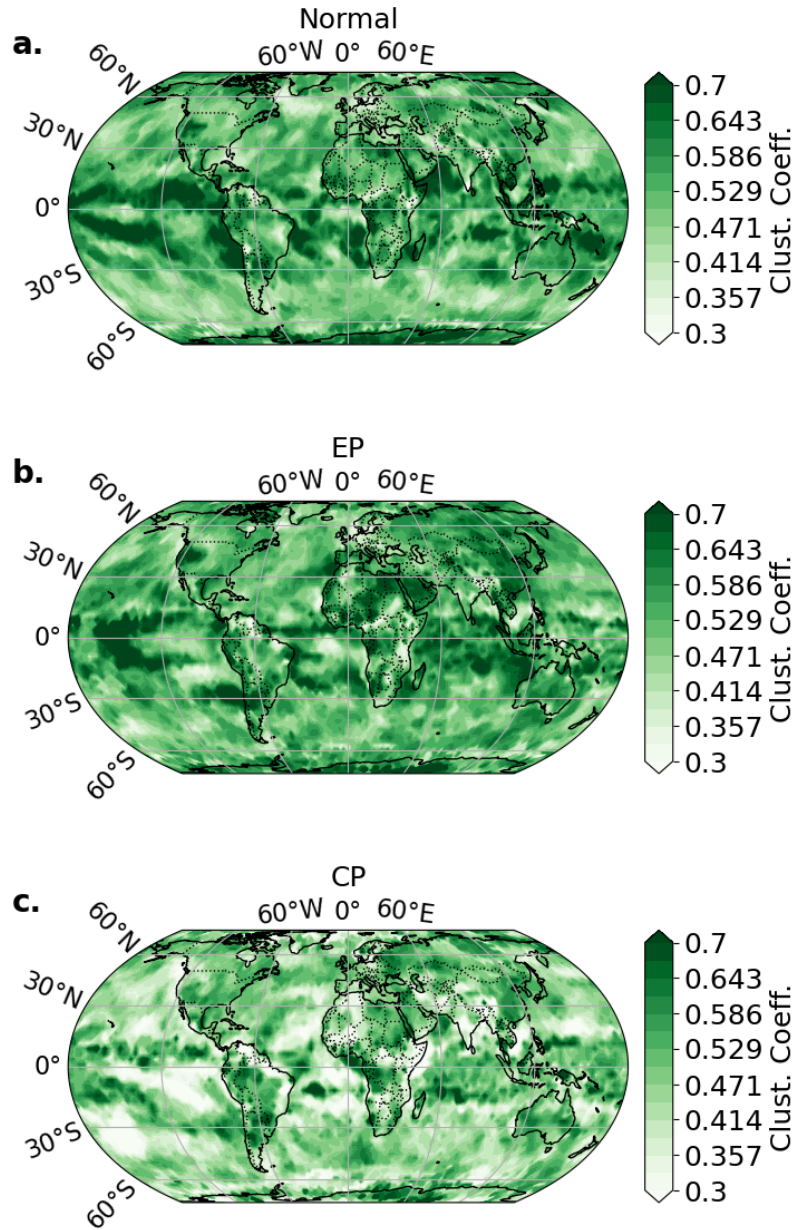


Figure 8: **Clustering Coefficient for normal, EP and CP conditions.** The clustering coefficient is computed using Eq. 9. Networks are obtained for normal (a), EP (b) and CP (c) conditions.

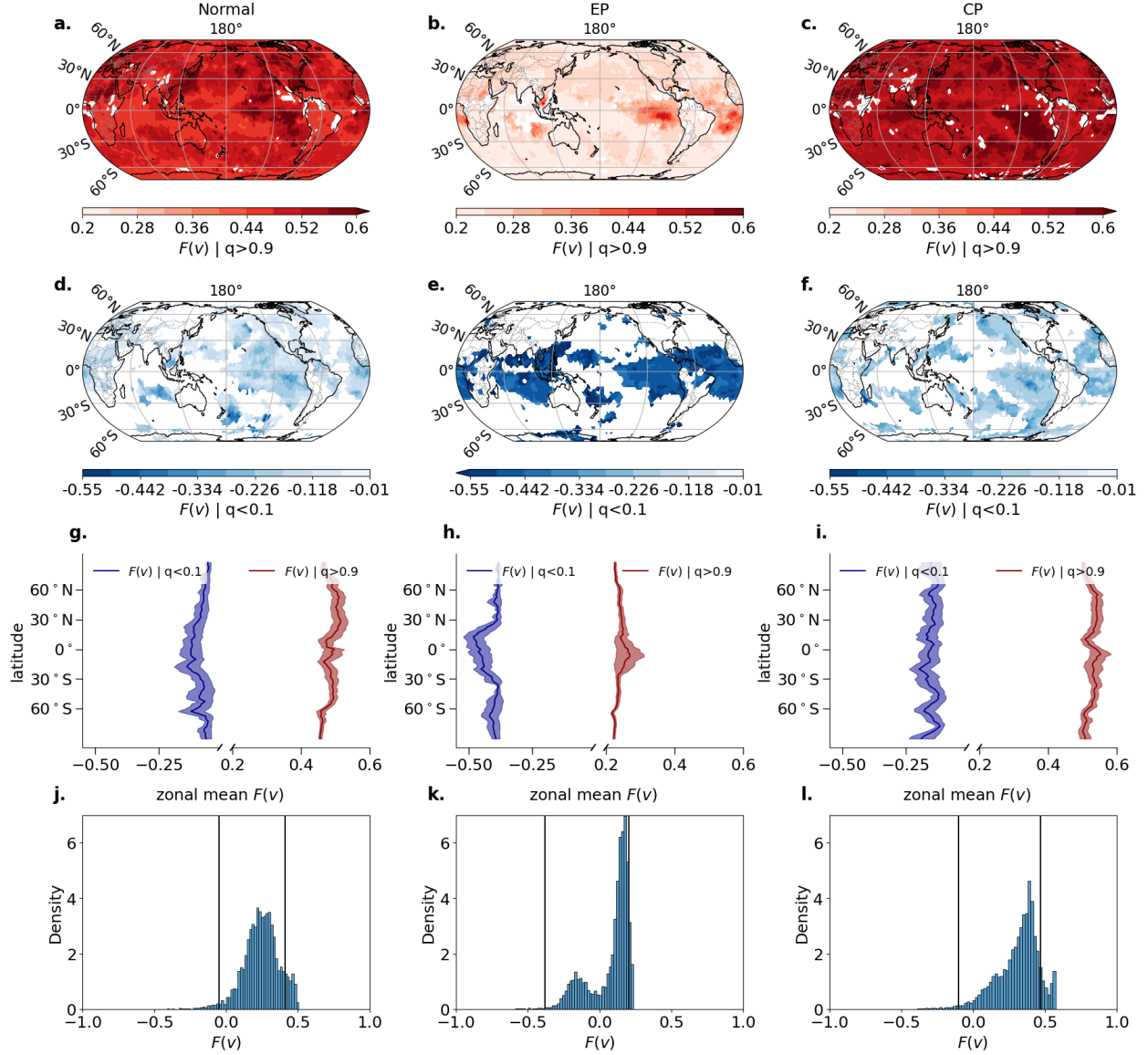


Figure 9: **Same as Fig. 3 but with equal scales.** The network curvature scales are fixed between the networks (a-i). The differences between the distributions of node curvature \tilde{f}_i of normal (j), EP (k) and CP (l) networks could be attributed to their network topologies. The quantiles $Q_F(0.1)$ and $Q_F(0.9)$ are indicated by black lines (j-l). In order to plot the quantiles of node curvature we have to adapt the scales, as done in the main text Fig. 3.

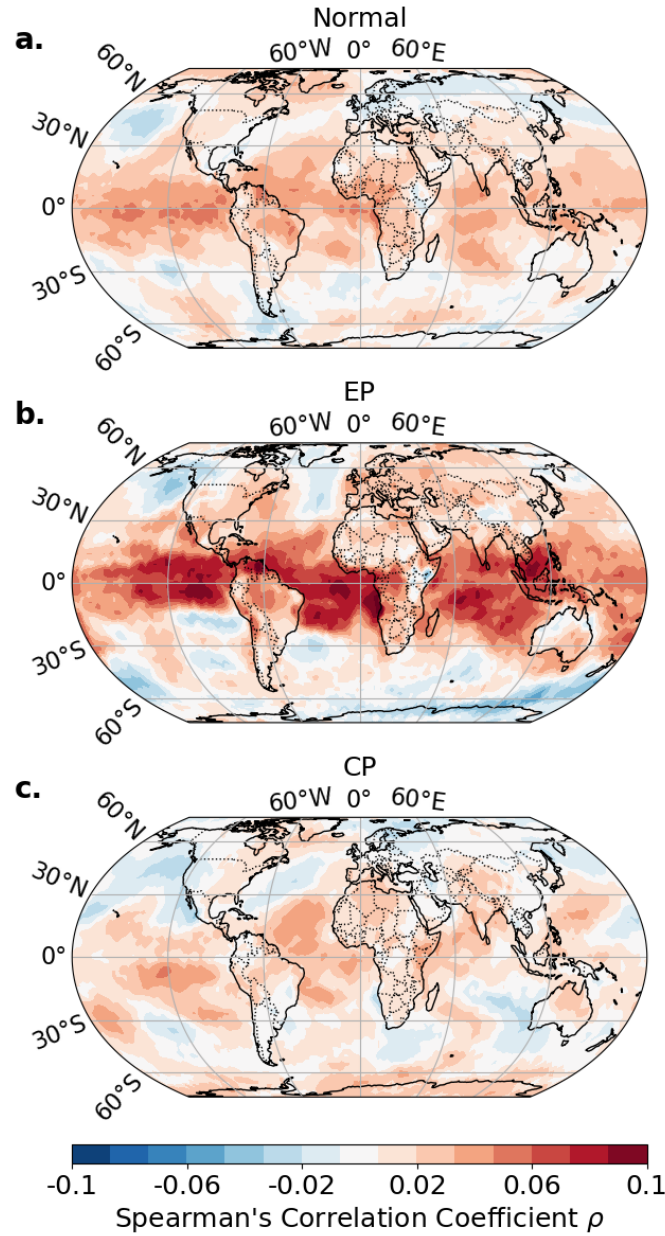


Figure 10: **Average Spearman's correlation coefficient.** SAT time series at one location is Spearman-correlated against all other time series of the global dataset. The average Spearman's correlation coefficient is shown for the climate networks constructed based on normal (a), Eastern Pacific El Niño (b) and Central Pacific El Niño (c) conditions.

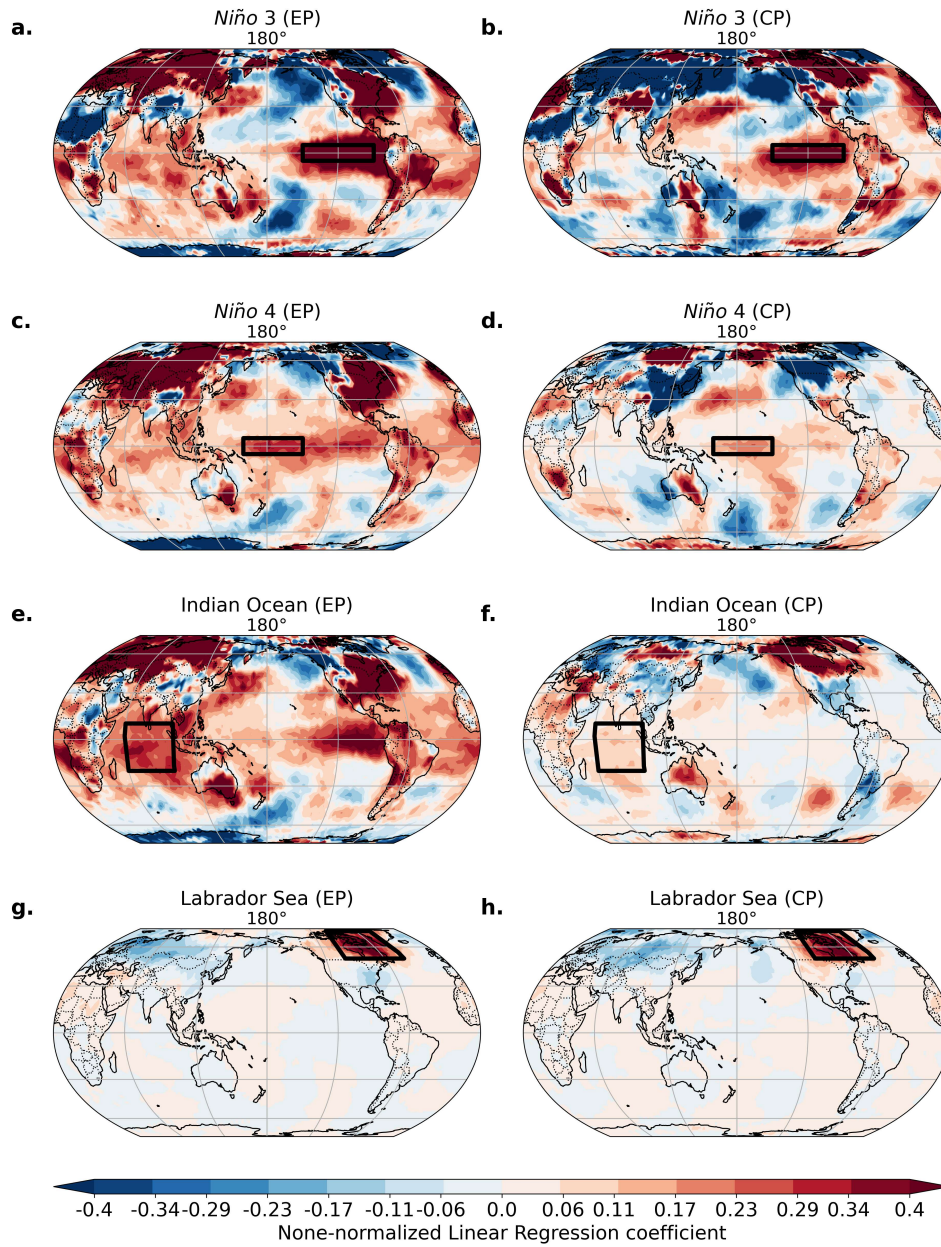


Figure 11: **SAT fields regressed on temperatures from the four selected regions.** SAT time series (not normalized) at each location is regressed against all the rank-normalized SAT time series inside the four regions (black rectangles). Displayed are the Niño 3 box (1. row), Niño 4 box (2. row), Indian Ocean (3. row), and Labrador Sea (4. row), with first column denoting EP and second column CP conditions.

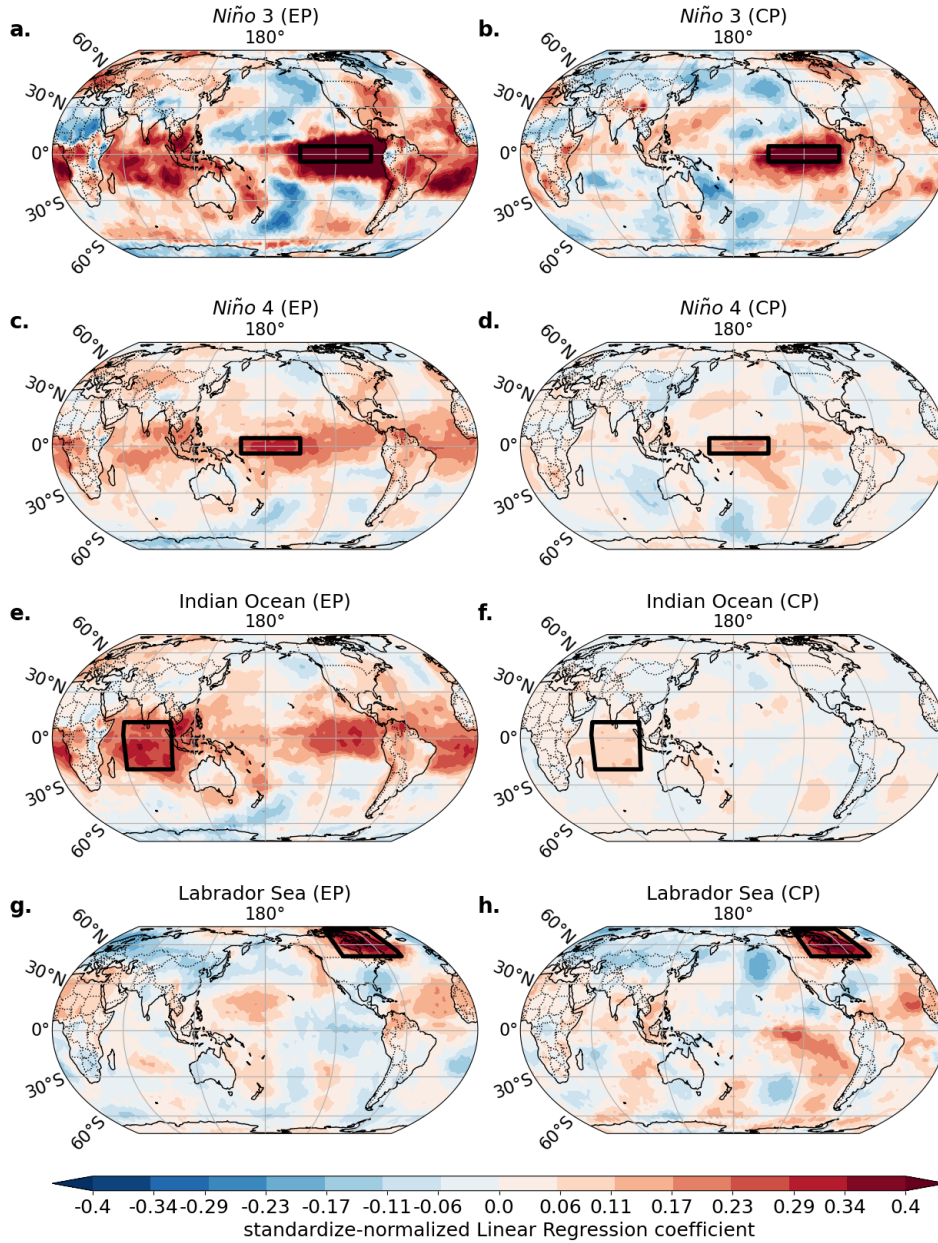


Figure 12: SAT fields (Z-score normalized) regressed on temperatures from the four selected regions. SAT time series at each location is regressed against all the rank-normalized SAT time series inside the four regions (black rectangles). Displayed are the Niño 3 box (1. row), Niño 4 box (2. row), Indian Ocean (3. row), and Labrador Sea (4. row), with first column denoting EP and second column CP conditions.

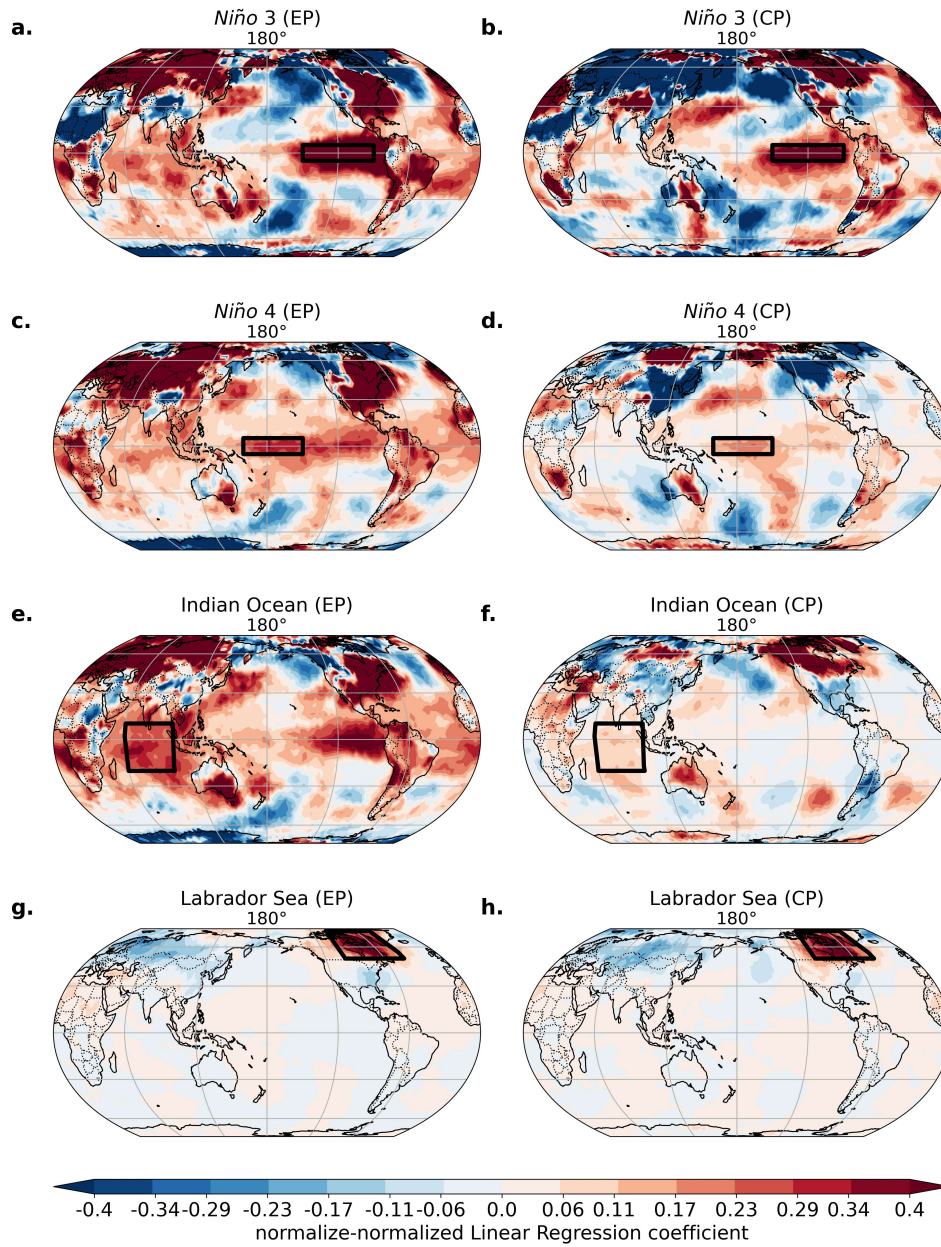


Figure 13: SAT fields (min-max normalized) regressed on temperatures from the four selected regions. SAT time series at each location is regressed against all the rank-normalized SAT time series inside the four regions (black rectangles). Displayed are the Niño 3 box (1. row), Niño 4 box (2. row), Indian Ocean (3. row), and Labrador Sea (4. row), with first column denoting EP and second column CP conditions.